

Galaxy Formation with local photoionisation feedback I. Methods

R. Kannan^{1*}, G. S. Stinson¹, A. V. Macciò¹, J. F. Hennawi¹, R. Woods², J. Wadsley², S. Shen³, T. Robitaille¹, S. Cantalupo³, T. R. Quinn⁴, C. Christensen⁵

¹Max-Planck-Institut für Astronomie, Königstuhl 17, 69117, Heidelberg, Germany

²Department of Physics and Astronomy, McMaster University, Hamilton, Ontario, L8S 4M1, Canada

³Department of Astronomy & Astrophysics, UCO/Lick Observatory, University of California, 1156 High St, Santa Cruz, CA 95064, USA

⁴Astronomy Department, University of Washington, Box 351580, Seattle, WA, 98195-1580, USA

⁵Department of Astronomy, University of Arizona, 933 North Cherry Avenue, Rm. N204, Tucson, AZ 85721-0065, USA

22 January 2018

ABSTRACT

We present a first study of the effect of local photoionising radiation on gas cooling in smoothed particle hydrodynamics (SPH) simulations of galaxy formation. We explore the combined effect of ionising radiation from young and old stellar populations. The method computes the effect of multiple radiative sources using the same tree algorithm used for gravity, so it is computationally efficient and well resolved. The method foregoes calculating absorption and scattering in favour of a constant escape fraction for young stars to keep the calculation efficient enough to simulate the entire evolution of a galaxy in a cosmological context to the present day. This allows us to quantify the effect of the local photoionisation feedback through the whole history of a galaxy’s formation. The simulation of a Milky Way-like galaxy using the local photoionisation model forms $\sim 40\%$ less stars than a simulation that only includes a standard uniform background UV field. The local photoionisation model decreases star formation by increasing the cooling time of the gas in the halo and increasing the equilibrium temperature of dense gas in the disc. Coupling the local radiation field to gas cooling from the halo provides a *preventive* feedback mechanism which keeps the central disc light and produces slowly rising rotation curves without resorting to extreme feedback mechanisms. These preliminary results indicate that the effect of local photoionising sources is significant and should not be ignored in models of galaxy formation.

Key words: atomic processes – galaxies: formation – galaxies:ISM – hydrodynamics – methods: N-body simulation – plasmas

1 INTRODUCTION

Within the current paradigm of galaxy formation theory, dark matter first collapses into small haloes, which merge to form progressively larger haloes. Galaxies form out of the gas that cools into the centres of these dark matter haloes and forms stars (White & Rees 1978; Mo et al. 2010).

Gas collapses into the dark matter haloes by radiating away its energy. Since angular momentum is conserved, the gas settles into a rotating disc from which stars form. Radiative cooling controls the infall of gas onto the disc, making it one of the most important processes of galaxy

formation. A number of factors slow the infall of gas including thermal pressure (Rees & Ostriker 1977; Binney 1977) and the incident radiation field (Rees 1986; Efstathiou 1992; Cantalupo 2010; Gnedin & Hollon 2012). Accurately modelling the cooling rate of halo gas is critical to determining how much fuel is available to form stars in the galaxy.

Gas cooling (Λ) depends most strongly on gas density ($\Lambda \sim n^2$), metallicity and the ionisation state. The local gas hydrodynamics determines the gas densities while chemical enrichment from stellar evolution determines the metallicity. The gas ionisation state depends on the temperature of the gas and on the incident radiation field from stars, Active Galactic Nuclei (AGN) and other radiation sources. In most galaxy formation models (including numerical hy-

* Email: kannan@mpia.de

drodynamical simulations), a uniform background is used to represent this radiation field. This background evolves with redshift according to the cosmic star formation and quasar luminosity histories (Haardt & Madau 2012).

Rees (1986) and Efstathiou (1992) showed that photoionisation can prevent gas from cooling into low mass halos. Wiersma et al. (2009) presented more detailed results that measured the effect of a uniform photoionisation background on individual ion species. Gnat & Ferland (2012) extended this analysis to include a variety of radiation fields that could vary due to proximity to galaxies. Oppenheimer & Schaye (2013a,b) explored the problem with a full chemical network including all the ionisation states of 30 elements in typical parcels of gas in the intergalactic medium (IGM) and found that the time it takes for gas to reach ionisation equilibrium can lead to significant changes in the state of gas in the IGM.

Cantalupo (2010) explored analytically the effect of local sources of radiation on the cooling of halo gas including the soft X-ray emission produced by star formation events, a component that is absent within typical stellar population synthesis models such as Starburst99 (Leitherer et al. 1999) (SB99) that only considers the blackbody radiation from young massive stars. Such low energy photons do not affect the cooling rate of high metallicity gas. However, massive stars are also strong X-ray sources due to their stellar winds, supernova remnants and binary interactions. When the high energy radiation from these sources is included in gas cooling models, their radiation can ionise the metals and can decrease the cooling rate of high metallicity gas considerably. Gnedin & Hollon (2012) created a general model for cooling in the presence of a radiation field near a galaxy (including both stars and AGNs). They showed that for a sufficiently general variation in the spectral shape and intensity of the incident radiation field, the cooling and heating functions can be approximated based only the photoionization rates of a few important coolants.

In this paper, we follow the lead of Cantalupo (2010) and Gnedin & Hollon (2012) in an attempt to self consistently include local ionisation sources, in addition to the uniform background of Haardt & Madau (2012), in cosmological simulations of galaxy formation.

One of the great challenges for including the effect of photoionisation in simulations is the need to trace the radiation as it propagates through the simulated volume. The radiation field at any given point is dependent on the brightness and distance to the source as well as the frequency dependent optical depth of the material between the source and sink. This makes the problem more expensive than the $\mathcal{O}(N^2)$ direct calculation of gravity.

Various solutions have been implemented for this complex computational problem. Gnedin (2008) used the local Sobolev approximation that calculates the column density from the density of a resolution element divided by the size of that element. Altay et al. (2008) (SPHRAY) and Pawlik & Schaye (2008) (TRAPHIC) both implemented sophisticated ray-tracing schemes in smoothed particle hydrodynamics (SPH) simulations. Altay & Theuns (2013) presented a recent update to SPHRAY. Petkova & Springel (2011) traced radiation through AREPO, a code that solves hydrodynamics on a moving mesh. For a review of how the different schemes perform in a variety of common test cases,

see Iliev et al. (2009). The codes all show that reionisation of the Universe happens in a non-uniform manner. While such radiative transfer schemes are useful tools for studying reionisation, these methods are so computationally demanding that it is impossible to evolve a cosmological simulation of galaxy formation much past $z = 4$.

Such models have been used in galaxies simulated to $z = 0$ in post-process. Fumagalli et al. (2011) solved radiative transfer on a high resolution grid to find that local radiation ionises low column gas, but has little effect on the statistics of Lyman limit and Damped Lyman alpha systems. Rahmati et al. (2013) used TRAPHIC post-process and found similar results. However, these studies do not yet explore the impact of the radiation field on the galaxy evolution.

Since it is as yet unclear what the effect of including local ionisation sources on galaxy evolution, we have decided to take a simple approach to the calculation of the radiative transfer, where possible. Our aim is to find a compromise between simulating a galaxy in a cosmological context from high redshift down to $z = 0$ and the precision of an on-the-fly radiative transfer calculation.

In a companion paper, Woods et al. (in prep) will present the details of the radiative transfer methods, which is here summarized in section 4.2. This paper describes how we calculate the cooling rates using that radiative transfer method and presents a preliminary simulation based on them. The paper is organized as follows: §2 presents the details of the cooling calculation. §3 describes the photoionisation sources we explicitly consider in our calculation. §4 outlines the approximations used in our radiative transfer approach while §5 describes the construction of the cooling table. Finally, in section §6 and §7 we present the results of our implementation of the local photoionisation feedback on a test gas particle and on a fully cosmological simulation of galaxy formation. Our conclusions are presented in §8.

2 GAS COOLING

A number of processes determine the internal heating (H) and cooling (Λ) rates in the hydrodynamic energy equation:

$$\frac{D\epsilon}{Dt} = -\frac{P}{\rho}\vec{\nabla}\cdot\vec{u} - \frac{1}{\rho}\vec{\nabla}\cdot\vec{F} + \frac{1}{\rho}\Psi + \frac{H - \Lambda}{\rho} \quad (1)$$

where ϵ represents the specific internal energy of a parcel of gas, $P\vec{u}$ represents the adiabatic work done on that gas, \vec{F} represents the flux of heat that is conducted out of the parcel, and Ψ represents the viscous dissipation rate.

Both the heating and cooling rates are a function of the density, n_i , of each ion species present in the gas parcel, as well as the parcel's temperature, T , and incident radiation field, J_ν :

$$\frac{H - \Lambda}{\rho} = f(n_i, T, J_\nu) \quad (2)$$

The density of each ion species is subject to a number of creation and destruction processes, which in turn also depend on n_j , T and J_ν :

$$n_i = f(n_j, T, J_\nu), j \neq i. \quad (3)$$

The densities of the ion species can be obtained using

networks of differential equations that account for all the electrons that are made available when atoms are ionised. Such networks can become arbitrarily complicated depending upon how many elements are included (Ferland et al. 1998; Gnat & Ferland 2012; Oppenheimer & Schaye 2013a). In simulations, it is possible to carry the ionisation state of every species from timestep to timestep to keep the non-equilibrium ionisation state of each element rather than making the assumption of ionisation equilibrium (eg. Oppenheimer & Schaye 2013b).

2.1 Primordial Cooling: non-equilibrium

Since these differential equations need to be solved for each particle during every timestep in a simulation, it becomes necessary to limit the calculation of non-equilibrium ionisation states to hydrogen and helium. We use the implementation of Shen et al. 2010 (see also Vogelsberger et al. 2013). Hydrogen and helium are the most abundant elements in the Universe, so their temperature and ionisation state are important in determining the dynamics and cooling of gas in simulations.

Primordial gas contains various ionisation states of hydrogen and helium: $i \in (\text{HI}, \text{HII}, \text{HeI}, \text{HeII}, \text{HeIII}, e^-)$. The rate of change of densities of these species are obtained by solving the following set of differential equations:

$$\frac{dn_{\text{HI}}}{dt} = \alpha_{\text{HI}} n_{\text{HI}} n_e - \Gamma_{e\text{HI}} n_e n_{\text{HI}} - \Gamma_{\gamma\text{HI}} n_{\text{HI}} \quad (4)$$

$$\frac{dn_{\text{HeI}}}{dt} = (\alpha_{\text{HeII}} + \alpha_d) n_{\text{HeII}} n_e - \Gamma_{e\text{HeI}} n_e n_{\text{HeI}} - \Gamma_{\gamma\text{HeI}} n_{\text{HeI}} \quad (5)$$

$$\begin{aligned} \frac{dn_{\text{HeII}}}{dt} = & \alpha_{\text{HeIII}} n_{\text{HeIII}} n_e + \Gamma_{e\text{HeI}} n_e n_{\text{HeI}} \\ & + \Gamma_{\gamma\text{HeI}} n_{\text{HeI}} - (\alpha_{\text{HeII}} + \alpha_d) n_{\text{HeII}} n_e \\ & - \Gamma_{e\text{HeII}} n_e n_{\text{HeII}} - \Gamma_{\gamma\text{HeII}} n_{\text{HeII}} \end{aligned} \quad (6)$$

where α_i is the *radiative* recombination coefficient for ion species i , α_d is the *dielectric* recombination coefficient, which only applies to HeII, Γ_{ei} is the *collisional* ionisation rate for each species, while $\Gamma_{\gamma i}$ is the photo-ionisation rate, defined as

$$\Gamma_{\gamma i} = \int_{\nu_{Ti}}^{\infty} \frac{4\pi J_{\nu}}{h\nu} \sigma_{\nu i} d\nu \quad (7)$$

where $\sigma_{\nu i}$ is the frequency dependant photoionisation cross section of the species ‘i’.

These equations are closed when combined with the following set of conservation equations:

$$n_{\text{HI}} + n_{\text{HII}} = n_{\text{H}} \quad (8)$$

$$n_{\text{HII}} + n_{\text{HeII}} + 2n_{\text{HeIII}} = n_e \quad (9)$$

The cosmic production of helium was constrained by Jimenez et al. (2003) using K dwarfs from Hipparcos catalog with spectroscopic metallicities and found that the amount of Helium produced compared to heavier elements in stars follows the relation: $\Delta Y/\Delta Z = 2.1 \pm 0.4$. In accordance with

this result we compute the helium abundance in the following manner:

$$Y_{\text{He}} = \begin{cases} (0.236 + 2.1Z)/4.0 & \text{if } Z \leq 0.1 \\ (-0.446(Z - 0.1)/0.9 + 0.446)/4.0 & \text{if } Z > 0.1 \end{cases}, \quad (10)$$

with the density of hydrogen being

$$Y_{\text{H}} = 1.0 - 4Y_{\text{He}} - Z, \quad (11)$$

where

$$Y_i = \frac{n_i M_{\text{H}}}{\rho} \quad (12)$$

where M_{H} is the mass of the hydrogen atom and ρ is the total density of the gas. Most of the radiative processes discussed above along with collisional excitation that causes the gas to cool, and the coefficients and the cooling rates are enumerated in Anninos et al. (1997).

In addition to determining the ionisation state of gas, the incident radiation field also injects energy into the gas when a high energy ($h\nu > h\nu_{\text{T}}$) photon, transfers the rest of its energy to the electron it frees from the atom. The photo heating rate is thus given by

$$H = n_{\text{HI}} \epsilon_{\text{HI}} + n_{\text{HeI}} \epsilon_{\text{HeI}} + n_{\text{HeII}} \epsilon_{\text{HeII}}, \quad (13)$$

where

$$\epsilon_i = \int_{\nu_{\text{T}}}^{\infty} \frac{4\pi J_{\nu}}{h\nu} \sigma_{\nu i} (h\nu - h\nu_{\text{T}}) d\nu \quad (14)$$

2.2 Metal cooling: equilibrium

A significant amount of cooling also occurs via elements heavier than hydrogen and helium. For these elements, we refrain from solving the entire non-equilibrium ionisation network due to its computational complexity. Instead, we assume equilibrium conditions hold and interpolate values in a look-up table as implemented in Shen et al. (2010). The table consists of heating and cooling rates as a function of total gas density, temperature, redshift, and the radiation fields from local sources, described in §3. Metallicity does not need to be a dimension in our table, since the cooling rate scales linearly with metallicity and can thus be easily calculated from the cooling rate of solar metallicity gas (see also Shen et al. 2010 and Vogelsberger et al. 2013).

Thus, our total cooling calculation is the summation of three components: i) non-equilibrium primordial - calculated on the fly in the code; ii) equilibrium metals - values tabulated from CLOUDY (v10.00, last described in Ferland et al. 1998); and iii) Compton scattering of CMB photons,

$$\Lambda_{\text{tot}} = \Lambda_{\text{H,He}} + \frac{Z}{Z_{\odot}} \Lambda_{\text{Z}_{\odot}} + \Lambda_{\text{c}}. \quad (15)$$

This division neglects some sources of free electrons in the cooling calculation. CLOUDY calculates the cooling rates of metals using the free electrons created in ionisation equilibrium primordial cooling. This number of free electrons may be different from the non-equilibrium primordial cooling in our code. Additionally, our non-equilibrium primordial cooling calculation assumes that the number of free electrons released from metals is negligible. Thus, our cooling calculation is a first approximation that can be improved by tracking non-equilibrium metal cooling in addition to H

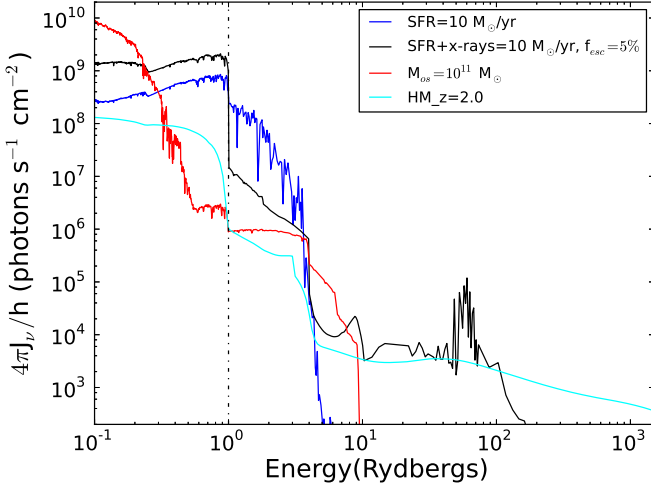


Figure 1. The incident photon flux from the photoionisation sources considered in our simulations. These fluxes are reported at 10 kpc from the source. The blue curve shows the photon flux as a function of energy from a population of young stars forming at the rate of $10 M_{\odot} \text{ yr}^{-1}$. The young stars have the highest photon flux at the hydrogen edge but decreases quickly at higher energy. The black curve shows the spectrum of young stars including the x-ray luminous cooling of shock-heated gas after a SNe event. The Spectral Energy Distribution (SED) of a $10^{11} M_{\odot}$, old (>200 Myr) stellar population is shown in red. Old stars emit fewer photons than young stars at the hydrogen edge, but has higher flux at higher energies ($h\nu > 4$ Rydberg). The cyan curve shows the UV background at $z = 2$. Compared to the plotted ionisation fields, this background flux is lower than local sources at low energies ($h\nu < 100$ Rydberg), but dominates at higher energies due to the hard photons emitted by AGN.

& He. It is worth noting that this assumption is used in practically all current numerical implementations of metal dependent gas cooling (Shen et al. 2010; Vogelsberger et al. 2013).

3 IONISING STELLAR RADIATION SOURCES

There are many radiation sources which produce high energy photons and ionise gas in the galaxy. In the following sections we outline the sources that we consider in our photoionisation model. One source of radiation not included in our model is quasars, since we do not follow the formation or gas accretion onto super massive black holes in our cosmological simulations. However, Vogelsberger et al. (2013) showed that the low frequency duty cycle of radiation from AGNs result in a minimal impact on the large scale gas dynamics in galaxies.

3.1 UV Background

Nearly all simulations include the effect of photoionisation from a uniform background. This UV background accounts for the UV radiation that all stars and AGN emit throughout the evolution of the Universe attenuated by the Lyman- α forest (Haardt & Madau 2012). Our refined method is an

attempt to account for more local ionising radiation. The Spectral Energy Distribution (SED) from Haardt & Madau (2012) (henceforth, HM) is shown as the cyan curve in Fig. 1. Since the HM SED incorporates the emission from AGNs, it contains photons up to x-ray energies, but the photon flux can be lower than local sources at energies less than 10 Rydbergs. We consider the HM SED as the minimum ionising flux seen by the gas particles in our simulations, at low redshift ($z < 9$).

3.2 Young Stars

Our initial spectral energy distribution (SED) for young stars comes from STARBURST99 (Leitherer et al. 1999) using an SED taken 10 Myr after stars start forming at a constant rate of $1 M_{\odot} \text{ yr}^{-1}$ using the “present day” (Eq. 6) IMF from Kroupa (2001) (blue curve in Fig. 1). The SED has a relatively high photon flux at the hydrogen edge (13.6 eV) but the flux drops precipitously to higher energies, with almost no flux above the helium edge (4 Rydbergs = 54.4 eV).

Fig. 2, shows how the cooling (solid curves) and heating (dashed curves) rates change in the presence of various levels of the radiation field (SFR= $1 M_{\odot} \text{ yr}^{-1}$, blue curve; SFR= $100 M_{\odot} \text{ yr}^{-1}$, black curve) from young stars compared to the cooling and heating rates in the presence of the peak HM radiation field (red) at $z = 2$. The gas used to make these cooling curves has a density of $n_H = 0.01 \text{ cm}^{-3}$, a metallicity of $Z = 0.01 Z_{\odot}$ and is at a distance 10 kpc from the star forming region. The cooling curve is calculated using the assumption that the gas in between the source and the gas test particle is optically thin. Thus, the flux is inversely proportional to the of the distance squared. All test cooling curves presented in this section were calculated using the code CLOUDY, which assumes photoionisation equilibrium for all elements.

The STARBURST99 young star SED suppresses hydrogen cooling that dominates in $\sim 10^4$ K gas. The spectrum also partially ionises some helium in strong radiation fields. It also slightly changes the equilibrium temperature of the gas. The equilibrium temperature is defined as the temperature where cooling transitions to heating because of the incident radiation file. Practically, it corresponds to the temperature at which the heating and cooling rates are equal. At temperatures above equilibrium, the gas cools, while at lower temperatures, it heats up. So, the equilibrium temperature depends on the shape of the heating and cooling curves.

Radiation fields change the heating and cooling curve depending on the energy of photons they possess. HM has the most high energy photons, whose extra energy results in heating, so it has the highest heating rates, but is has a low flux at low energies (1 – 10 Rydbergs) causing minimal impact on the cooling of low metallicity gas. The young star blackbody spectrum includes mostly photons around the hydrogen ionisation edge, so it results in minimal heating, but a large reduction in the cooling rate. The net result is that the radiation from new stars, for typical values of radiation field in the galaxy, is more effective at raising the equilibrium temperature of the gas than the background HM UV spectrum.

Fig. 3 shows the effect of metallicity on the cooling function at a fixed star formation rate of $10 M_{\odot} \text{ yr}^{-1}$. While this

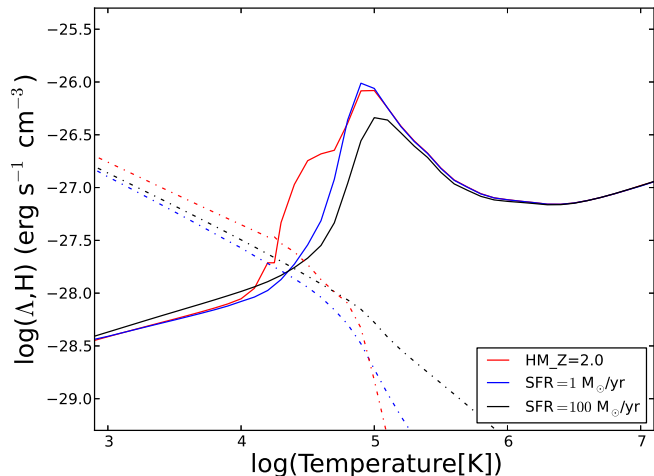


Figure 2. The cooling (solid) and heating (dashed) rate curves of gas in the blackbody radiation field of young stars (STARBURST99) at two star formation rates compared to the cooling and heating in presence of the HM UV background spectra. The cooling rates are shown for gas with a density, $n_H = 0.01 \text{ cm}^{-3}$, metallicity, $Z = 0.01Z_\odot$, and a radiation source 10 kpc distant.

radiation field eliminates hydrogen cooling at solar metallicity (note the lack of a peak around 10^4 K in the red curve), heavier elements make cooling rates more than an order of magnitude higher than in the low metallicity gas (blue) at all temperatures. The higher cooling rates mean that the equilibrium temperature of the gas is also an order of magnitude lower in solar metallicity (red curve) gas because the heating rate does not change. Fig. 3 shows that cooling is most easily suppressed in low metallicity gas irradiated with a soft UV spectrum from young stars.

3.3 X-rays from Young Stars

Cantalupo (2010) considered the radiation from young stellar populations, including both the blackbody radiation from hot young stars and the X-rays that supernovae remnants emit. Using analytic calculations, Cantalupo (2010) showed that while stellar photons ionise hydrogen, soft X-rays ionise other significant metal coolants. The x-ray photoionisation increased the equilibrium temperature, which consequently slowed the accretion of gas onto the disc.

X-rays are produced in a number of ways. Rapidly outflowing gas from stellar winds or supernova explosions shocks against the interstellar medium (ISM) and thermalises (Heckman et al. 1995; Strickland et al. 2004). Non-thermal processes associated with supernovae explosions and high mass X-ray binaries also emit x-ray radiation (Grimm et al. 2003; Persic et al. 2004).

We use the SED for a 5 Myr old stellar population (Fig. 1, black curve) from Cerviño et al. (2002). The Cerviño et al. (2002) SEDs are derived from models of young O and B stars and the X-rays that their stellar winds and supernova explosions produce. Their models are calibrated to match the observed relationship between SFR and soft X-rays (for eg. see Heckman et al. 1995). In their models,

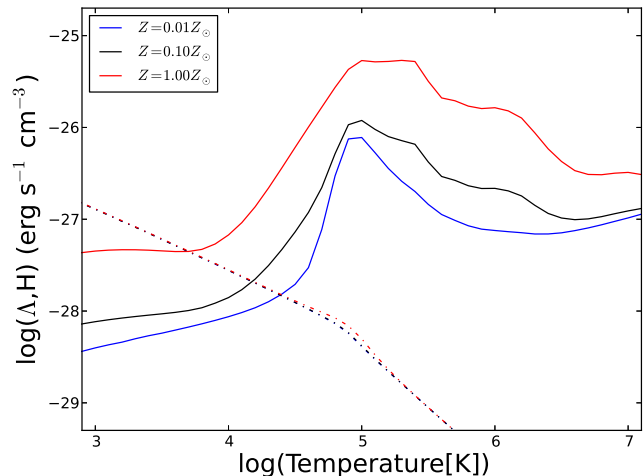


Figure 3. Cooling function as in Fig. 2 of gas at a variety of metallicities in a radiation field 10 kpc away from a stellar population forming stars at $10 M_\odot \text{ yr}^{-1}$. This young population only emits radiation to the helium edge (4 Rydberg), so only the hydrogen cooling at $T < 10^5 \text{ K}$ is reduced. The increase in cooling in higher metallicity gas in the range $10^4 < T < 10^5$ is due to an increasing presence of heavy metal coolants such as O, Ne and Fe. The heating rate remains constant because the radiation field is the same for all three curves.

the X-ray emission peaks when the stellar population is ~ 5 Myr old and continues for ~ 100 Myr. To simplify our calculation, we use the SED of a 5 Myr old stellar population for all stars younger than 10 Myr, so we pick the maximum emission SED, but only use it for one-tenth of the time that x-rays are emitted. Following Cantalupo (2010), we assume that 5% of the mechanical energy from the SNe is emitted as X-rays.

The Cerviño et al. (2002) models assume a Salpeter IMF, but our simulations use a Chabrier (2003) IMF that has more stars with $M_\star > 8 M_\odot$. So, we renormalise the Cerviño et al. (2002) SED to make the flux from O & B stars and the number of subsequent SNe events consistent with the Chabrier IMF.

There is significant absorption of Lyman continuum photons in the galaxy due to the abundance of hydrogen. To include this effect we assume an escape fraction of 5% around Lyman-limit frequencies to mimic the highly absorptive nature of their birth molecular clouds (e.g. Bergvall et al. (2006), see section 4.1 for a more thorough discussion on the escape fraction).

Fig. 4 shows how including X-rays in the young star SED affects the cooling curve in $Z = Z_\odot$ gas at 10^{-2} cm^{-3} density at 1 kpc from the star formation site. At high metallicity, the young star SED without X-rays (thin curves) only eliminates hydrogen cooling, independent of the star formation rate of the galaxy. The harder x-ray spectrum (thick curves) ionises heavier elements such as oxygen, neon and some ions of iron to lower the gas cooling rate and also raise the heating rate of the gas. These effects combine to increase the equilibrium temperature by an order of magnitude. X-rays thus remain an important ionisation source at

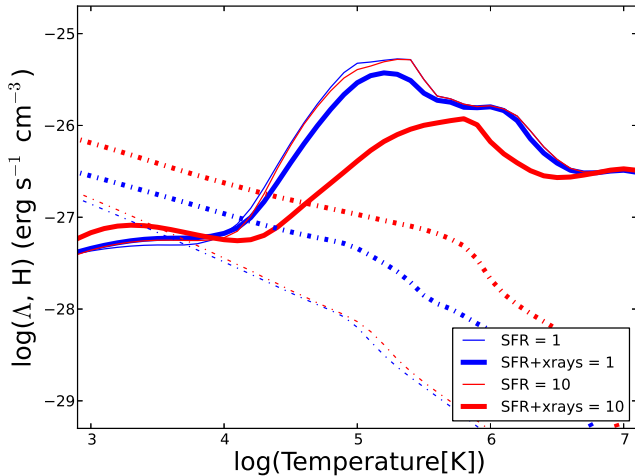


Figure 4. The cooling function as in Fig. 2, but now includes the effect of x-rays from young stellar populations (Cerviño et al. 2002). While blackbody radiation from young stars only quenches hydrogen cooling, the addition of x-rays stops cooling from many metal ion species and increase the heating rate considerably (see Cantalupo 2010).

low redshifts, where the halo gas has been metal enriched by continuous bursts of star formation. For this reason, we use an SED that combines the black body emission of young stars with the x-ray emission that massive stars produce in stellar winds and supernova explosions in our simulations. Henceforth, flux from young stars includes x-rays along with their black body spectrum.

3.4 Old Stars

Naively, old stellar populations seem like they should not be sources of ionising photons. Since all the hot young stars have exploded as supernovae, all that are left are cool, old stars. However, a UV upturn was observed coming from the old stellar population at the center of M31 (Code 1969), and was determined to be light from extreme horizontal branch stars. Subsequently, UV radiation has been detected from many quiescent, early type galaxies (Kaviraj et al. 2007). What fraction of this radiation is from young stars, forming at low rates, compared to how much is from old stars is still a question waiting to be answered with better observations. Additionally, recent UV telescopes like GALEX have only been able to detect relatively soft UV radiation sources. However stellar population synthesis models predict that stars that have shed their outermost envelopes, so called “post-AGB” stars, should emit a hard UV spectrum.

Bruzual & Charlot (2003) include such stars in the spectral energy distribution of a simple stellar population (SSP). The SED of SSPs older than 200 Myr is harder, though much fainter (at the hydrogen edge), than the UV SED for a young SSP. In the model, the photon flux increases near the helium edge, due to the accumulation of post AGB stars. The shape of the SED remains fairly constant from 200 Myr to 13 Gyr because low mass stars evolve within a narrow temperature range all the way from the main se-

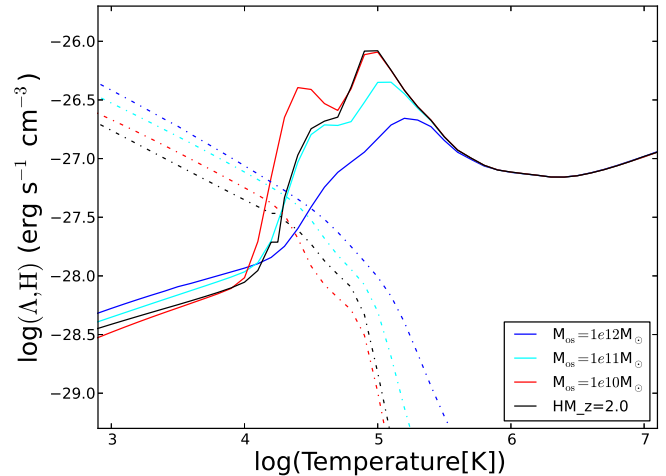


Figure 5. The heating and cooling functions for gas as in Fig. 2 irradiated by various masses of old ($t > 200$ Myr) stars. The SED is taken from Bruzual & Charlot (2003).

quence to the AGB phase. This implies that a constant SED can be used for old stars irrespective of their age (Fig. 1, red curve). We choose the 2 Gyr SED since it is near the mean of the SEDs.

Fig. 5 shows the effect of the old star SED on the cooling function of gas as a function of intensity of the incident radiation field. The gas has the same conditions as that studied in §3.2 ($n_H = 0.01 \text{ cm}^{-3}$, $Z = 0.01 Z_\odot$, $d = 10 \text{ kpc}$). The radiation with energies higher than the helium edge can eliminate helium cooling in the gas. A galaxy with $M_\star = 10^{10} M_\odot$ has less effect on the cooling function than the peak HM UV background ($z = 2$) because its ionising flux is so low. $10^{11} M_\odot$ stars produce a strong enough radiation field to reduce cooling below the HM level. Thus, radiation from old stars starts to play a role in massive galaxies, where the radiation field is strong, and at lower redshifts, once the HM background has decreased from its peak. Thus, they might help limit star formation in massive elliptical galaxies.

The consequences of photoionisation that are most critical for galaxy formation are the decrease in the cooling rate of the gas and the increase in the equilibrium temperature, which is the minimum temperature to which gas can cool. Moreover, the equilibrium temperature sets the minimum pressure a gas parcel can reach. More intense and harder radiation fields shift the equilibrium temperature higher, while higher densities and metallicities shift the equilibrium temperature lower.

4 CALCULATING THE RADIATION FIELD

In the previous section, the different sources of local ionising radiation were enumerated and shown to be important in the calculation of gas cooling in galaxies. However, propagating the radiation from the sources to the gas particles can become computationally expensive (e.g. Altay et al. 2008). This necessitates the use of some simplifying, albeit physically motivated, assumptions. We plan to relax these

assumptions in future work in order to present a more complete implementation of radiative transfer.

4.1 Escape Fractions

Our strongest assumption is that the gas is optically thin to photons so that the optical depth is determined simply by the escape fraction of ionising photons from the interstellar medium (ISM). Given the abundance of neutral hydrogen in the Universe, Lyman continuum photons with around 1 Rydberg of energy will generally see high optical depths and thus have short travel distances and low escape fractions. In future work, we will try to improve our model to make more physical calculations for the optical depth. For now, we assume that since young stars form embedded in molecular clouds, the photoionising escape fraction, f_{esc} , is low ($f_{esc} \sim 5\%$). This number is an upper limit, motivated by a number of observations (Bergvall et al. 2006; Grimes et al. 2009; Steidel et al. 2001; Shapley et al. 2006; Siana et al. 2007; Nestor et al. 2013). The escape fraction we use is frequency dependent (f_{esc}^ν), similar to Cantalupo (2010),

$$f_{esc}^\nu = [f_{esc}^{LL} + (1 - f_{esc}^{LL})e^{-\tau_\nu}] \quad (16)$$

where f_{esc}^{LL} is the absolute escape fraction at the Lyman Limit, $\tau_\nu = \sigma_\nu N(H^0)$ is the neutral hydrogen optical depth and σ_ν the corresponding cross-section. Our 5% escape fraction means that we fix $f_{esc}^{LL} = 0.05$. The value of $N(H^0)$ determines the hardening of the spectrum around the Lyman Limit. We anticipate that this parameter has a little effect on our results and we fix $N(H^0) = 10^{20} \text{ cm}^{-2}$. Escape fractions are a strong function of the distance from the source. $f_{esc} = 5\%$ represents the mean escape fraction at our spatial resolution $\sim 300 \text{ pc}$. For old stars, we assume that they have left their dense birth locations and that the escape fraction of their ionising photons is 100%.

4.2 Combining Sources

Each parcel of gas will receive a ionising flux from *all* the radiation sources (stars in our case) with an intensity proportional to the inverse of the distance square. In order to reduce the computational cost of the distance calculation, we exploit the tree algorithm used to compute the gravitational force, which already groups sources according to their distance from the gas particle.

Our grouping scheme is a first rough attempt at calculating radiative transfer. Woods et al. (in prep) will present the radiation transfer method in more detail. Our initial attempt takes little account of absorption except for the constant escape fraction used for young stars described above.

Combining sources of the same kind is an algebraic operation, since the SEDs do not evolve with time, so the summation of SEDs only affects their normalisation. In this manner, the radiation field incident on a gas particle is calculated using two separate components, one from young stars (ϕ_{SFR}) and one from old stars (ϕ_{os}). Young stars in our scheme are all those with an age $< 10 \text{ Myr}$, while old stars have an age

$> 200 \text{ Myr}$.¹ For each gas particle, the effective flux, ϕ , is the sum of the sources normalized by the distance from the gas particle squared, as follows:

$$\phi_{\text{SFR}} = \frac{1}{10^7 \text{ yr}} \sum_{i=1}^N \frac{M_i(t < 10 \text{ Myr})}{(r_i \text{ kpc})^2} \quad (17)$$

$$\phi_{\text{os}} = \sum_{i=1}^N \frac{M_i(t > 200 \text{ Myr})}{(r_i \text{ kpc})^2} \quad (18)$$

with the total photoionisation and heating rates, for each species ‘i’, given by

$$\Gamma_{\gamma i} = \phi_{\text{SFR}} \Gamma_{\gamma i, \text{SFR}} + \phi_{\text{os}} \Gamma_{\gamma i, \text{os}} + \Gamma_{\gamma i, \text{HM}} \quad (19)$$

$$\epsilon_i = \phi_{\text{SFR}} \epsilon_{i, \text{SFR}} + \phi_{\text{os}} \epsilon_{i, \text{os}} + \epsilon_{i, \text{HM}}. \quad (20)$$

Here, $\Gamma_{\gamma i, \text{SFR}}$ and $\epsilon_{i, \text{SFR}}$ are normalised to a radiation field 1 kpc away from a population forming stars at a rate of $1 M_\odot \text{ yr}^{-1}$. These quantities are calculated using Eqs. 7 and 14, with the SED of these stars taken from Cerviño et al. (2002) (see §3.3). Similarly, $\Gamma_{\gamma i, \text{os}}$ and $\epsilon_{i, \text{os}}$ are normalised based on a radiation field 1 kpc away from a $> 200 \text{ Myr}$ stellar population with a mass of $1 M_\odot$. For the old stars the SED is taken from Bruzual & Charlot (2003) as mentioned in §3.4. $\Gamma_{\gamma i, \text{HM}}$ and $\epsilon_{i, \text{HM}}$ are the UV background photoionising and photo heating rates, which are redshift dependent and taken from Haardt & Madau (2012). The cooling table uses separate values for ϕ_{SFR} , ϕ_{os} , and redshift in addition to temperature and density to determine the cooling rate for the gas.

Therefore, the photoionisation rate, Γ , and the heating rate, ϵ , for each species (i), used in the non-equilibrium calculation can simply be summed as shown in Eq. 19 & 20. The details about how the distance (r_i) is calculated will be presented in Woods et al. (in prep) (For a short description see §7).

5 COOLING TABLE CREATION

As shown in Eq. 15, the total gas cooling is divided into primordial, metal and Compton cooling. The primordial and Compton cooling is calculated on-the-fly as described in §2.1. However, to reduce the complexity of the cooling calculation as the simulation runs, the metals are assumed to be in ionisation equilibrium and their heating and cooling rates are tabulated across a range of physical conditions using CLOUDY. This look up table is used in the simulations.

The table has four dimensions at $z > 9$ and five dimensions thereafter. The four common dimensions are density, temperature, ϕ_{SFR} and ϕ_{os} . After $z = 9$, the UV background turns on so a redshift dimension is added to track how the HM SED shape changes. We make the division at $z = 9$, even though Haardt & Madau (2012) tabulate the UV background to $z = 15$, in order to limit the size of the cooling

¹ No flux from stars in between these two ages is considered, in agreement with results from Bruzual & Charlot (2003)

table. The mean free path of photons at high redshift is low because the Universe is not yet reionised, so the flux of the background UV field is relatively low. There is never a metallicity dimension in the table as cooling is assumed to scale linearly with metallicity as discussed in §2.2.

In both parts of the cooling table, the density ranges from 10^{-9} cm^{-3} to 10^4 cm^{-3} with a spacing of 0.5 dex in log space. The temperature ranges from 10^2 K to 10^9 K with a resolution of 0.1 dex. At $z > 9$, ϕ_{SFR} ranges from 10^{-11} to $10^2 \text{ M}_{\odot} \text{ yr}^{-1} \text{ kpc}^{-2}$ with a resolution of 0.5 dex, and ϕ_{os} ranges from 10 to $10^{10} \text{ M}_{\odot} \text{ kpc}^{-2}$ also with a resolution of 0.5 dex. These minimum values correspond to the CIE cooling rates, while the maximum values correspond to the maximum star formation rate and mass of high redshift galaxies. For $z \leq 9$, ϕ_{SFR} covers a smaller range, 10^{-5} to $10^3 \text{ M}_{\odot} \text{ yr}^{-1} \text{ kpc}^{-2}$ with a resolution of 0.5 dex. ϕ_{os} ranges from 10^6 to $10^{12} \text{ M}_{\odot} \text{ kpc}^{-2}$ with 0.5 dex spacings. The minimum values are higher at $z \leq 9$ because the HM UV background sets the minimum rather than collisional ionisation equilibrium. The maximum SFR and mass are increased to reflect observations. The redshift dimension that accounts for the UV background ranges from 9.0 to 0.0 with a resolution of 0.5. The resolutions were motivated by Gnedin & Hollon (2012).

To create the table, cooling and heating rates are calculated at every point for solar and primordial metallicity gas using CLOUDY. The difference between the solar and primordial metallicity values is stored as the heating and cooling rates due to the metals only. The values are stored as natural logarithms with single point precision, which provides accurate values, and limits the size of the table to 78 MB, a size well within the memory capacity of modern computer hardware.

6 TEST PARTICLE EVOLUTION

The methods described in the previous sections are implemented in the smoothed particle hydrodynamics (SPH) code GASOLINE first described in Wadsley et al. (2004). As a first test of the cooling implementation, we calculate the evolution of the temperature and ionisation state of a single isolated particle over the course of 350 Myr. The particle stays at a constant density and metallicity since it is not part of a fully dynamic simulation. The effects of dynamics are explored in a full simulation in §7.

Fig. 6 shows the evolution of a gas particle with a density $n_H = 0.001 \text{ cm}^{-3}$ in a young star radiation field that includes x-rays as described in §3.3. Unlike for the cooling curves in §3 that showed the effect of the stellar fields and HM separately, now their fields are combined as described in §4.2. The effect of the background UV field alone is shown as the blue curve. The distance from the source to the test gas particle is 10 kpc. The left column shows how the particle cools when its metallicity is $0.01 Z_{\odot}$, similar to unenriched gas falling for the first time into a galactic halo (Brook et al. 2013). The right column shows the particle cooling time when its metallicity is $0.1 Z_{\odot}$, similar to gas that has cooled into the disc and has been ejected into the halo (Brook et al. 2013).

A comparison of the top two panels shows that cooling times are longer and the equilibrium temperatures are

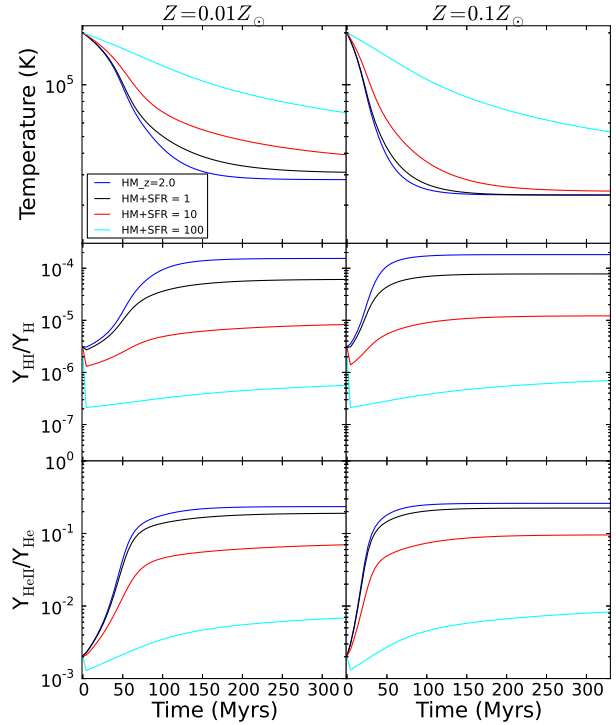


Figure 6. The effect of various star formation radiation fields on a parcel of gas with $n_H = 0.001 \text{ cm}^{-3}$ density. The gas cooling time and equilibrium temperatures increase significantly even for a high metallicity gas due to the presence of high energy x-ray photons.

higher in low metallicity gas. Compared to the HM line, the top right panel shows that X-rays also prolong cooling at $0.1 Z_{\odot}$, though to a lesser extent than at $0.01 Z_{\odot}$. The lower four panels show that the young star radiation fields keep hydrogen and helium ionised even after the gas cools. What is not shown in the ionisation plots is that they can also ionise other potential metal coolants.

For each metallicity, stronger radiation fields reduce the neutral hydrogen and HeII fractions (middle and bottom panels). In the $0.01 Z_{\odot}$ case, the lack of metals means that the delayed cooling is primarily due to the ionisation of hydrogen and helium. While the fractions of neutral hydrogen and HeII are similar between the $0.01 Z_{\odot}$ and $0.1 Z_{\odot}$ with the same ionisation field, the cooling rate in $0.1 Z_{\odot}$ is higher. The faster cooling is due to metal coolants more prevalent in the $0.1 Z_{\odot}$ gas. Since metal cooling is computed using equilibrium gas in CLOUDY, it is impossible to show the ionisation state of the metal coolants in our current test particle runs (but see Oppenheimer & Schaye 2013a).

Fig. 7 shows the evolution of the same particles in the old star radiation field. Old stars have a smaller effect than young stars that include X-rays, especially in high metallicity gas. The HeII fractions (bottom panels) are systematically lower in the old star radiation field (Fig. 7) than in the young star field (Fig. 6) because the flux at energies just above the helium ionising edge is higher. While old stars ionise helium, they do not ionise metals, so the gas

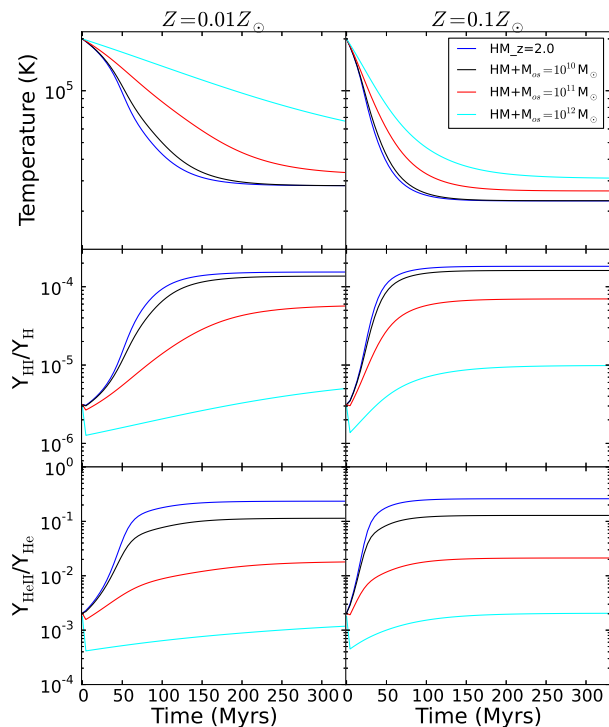


Figure 7. Same as Fig. 6, but in the radiation field created by old (>200 Myr) stellar populations of 3 different masses. The cooling time and the equilibrium temperature increases in the presence of a local radiation field from old stars, although not to such an extent as in radiation field from star formation.

cools faster at high metallicities than it does in young star radiation field.

7 COSMOLOGICAL SIMULATION USING LOCAL PHOTOIONISATION FEEDBACK

We want to study the effect of local ionising radiation on the whole process of galaxy formation in a cosmological context. For this purpose, we implement local photoionisation feedback in GASOLINE. The version of GASOLINE is the same described in Stinson et al. (2013) with the changes to cooling that have been described in the previous section.

7.1 Simulation physics

We select a galaxy from the McMaster Unbiased Galaxy Simulations (MUGS, Stinson et al. 2010) that has a halo mass of $6.4 \times 10^{11} M_{\odot}$. With the feedback prescription used in Stinson et al. (2013), the star formation rate of the galaxy increases steadily to $12 M_{\odot} \text{ yr}^{-1}$ at $z = 0$. This galaxy was chosen to show the maximum effect of the local photoionisation field. The galaxy has a gas mass resolution of $2 \times 10^5 M_{\odot}$ with a gravitational force softening of 310 pc.

The star formation and feedback model is the same as the fiducial simulation from the Stinson et al. (2013) parameter study. The star formation efficiency, c^* , is 0.1, and the density threshold is 9.3 cm^{-3} . The stellar population that

forms follows a Chabrier (2003) initial stellar mass function. Stellar feedback comes from type II supernovae (SNII) and pre-supernova energy (early stellar feedback, ESF hereafter). Each SNII explosion ejects $E_{SN} = 10^{51}$ erg of thermal energy into the surrounding ISM, which has its cooling delayed according to the blastwave solution presented in Stinson et al. (2006). This cooling delay typically lasts several Myr. Type II and Ia supernovae chemically enrich the ISM according to a detailed stellar evolution model as described in Stinson et al. (2013). Energy injection before SNII explosions (“early stellar feedback”) is modelled using 10% of the bolometric luminosity from young stars, an amount comparable to the UV flux. This energy is deposited directly into the gas surrounding the young stars as thermal energy, and then is rapidly radiated away.

We add our local photoionisation feedback to these stellar feedbacks. As outlined in §4.2, the contribution from stars are summed based on their distance from the gas particle for which we want to compute the incoming radiation. Close sources (stars) are treated as individual sources, while distant one are grouped based on the gravity tree. A detailed description of this method will be provided in Woods et al. (in prep).

We emphasize that the simulations presented here are preliminary. One concern is that we include the radiation energy from young stars twice, both as a photoionisation source and as a source of thermal energy for the early stellar feedback. Though the details of the pre-supernova thermal energy input would change, the energy could also be the hot gas created by stellar winds. In future models, we hope to present a more consistent picture. For now, we leave our model as similar as possible to our previous simulations so that the effect of including local photoionising radiation on the formation of the disc is apparent.

A second concern is that the effect of low energy photons in our simulations may be overestimated because the outer regions of high density gas clouds will shield the inner regions from the radiation field. This ‘self-shielding’ is important in gas with a density higher than 0.1 cm^{-3} (Ceverino et al. 2013). However, we have shown that the x-ray photons have the largest effect on cooling and these photons have a very small interaction cross section. So, ignoring self-shielding effects may be a reasonable first approximation.

7.2 Simulation results

We perform two simulations of the galaxy, one including the HM UV background only (hereafter, HM), and one adding local photoionisation feedback (LPF) to the UV background (HM+LPF).

Fig. 8 shows the star formation history of the two simulations. The star formation histories are nearly identical until $z \sim 1.5$, after which they diverge. The star formation rate in the HM run (red curve) steadily increases to $12 M_{\odot} \text{ yr}^{-1}$ at $z = 0$. The HM+LPF simulation (blue curve) maintains a steady star formation rate of $\sim 4 M_{\odot} \text{ yr}^{-1}$ from $z = 1.5$ until $z = 0$. The reduced star formation results in $\sim 40\%$ less stellar mass than in HM at $z = 0$.

To understand the physics behind the lower star formation rate in HM+LPF, Fig. 9 shows a comparison of the distribution of the gas in temperature–density phase space

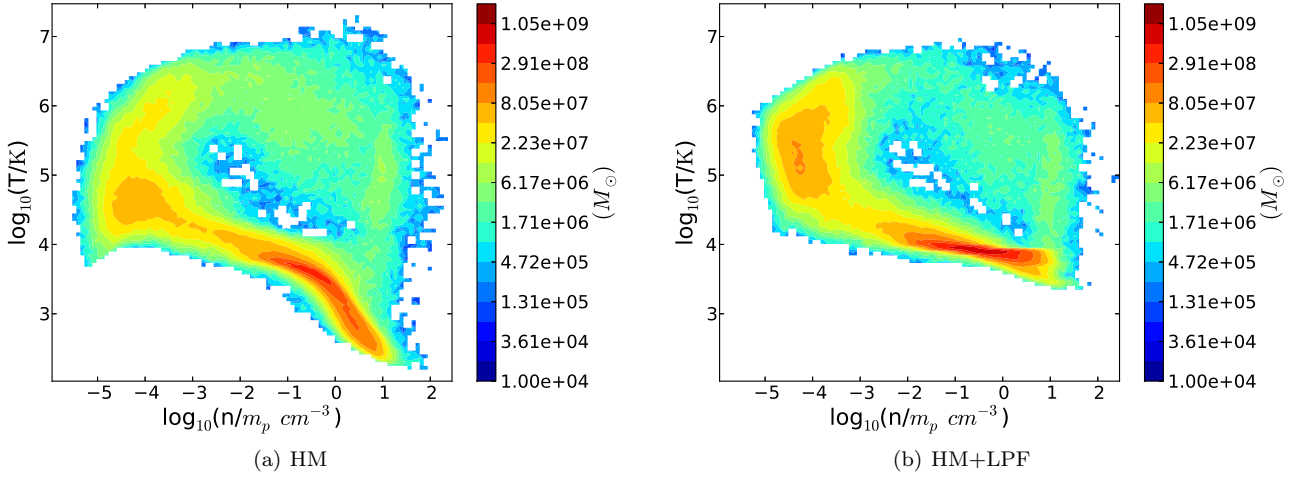


Figure 9. Temperature–density phase space diagrams present in a phase bin, 0.1 dex in temperature by 0.1 dex in density at $z = 0$. Three effects of local photoionization are visible: (i) High density, low temperature gas is absent in the presence of the local radiation field, (ii) The mass of gas accreting from the halo to the disc is reduced (gas channel from top left to bottom right) and (iii) the temperature of the hot halo gas around the galaxy is significantly higher.

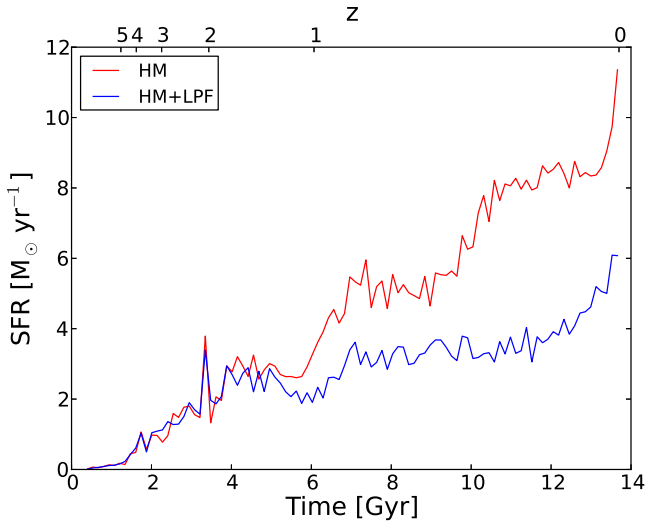


Figure 8. A comparison of the star formation histories for the two simulations. The star formation rates are similar until $z \sim 1.5$ and then they begin to diverge.

of the two simulations at $z = 0$. Three differences are apparent between the simulations: the mean temperature of low density halo gas, the amount of gas cooling out of the halo onto the disc, and the absence of very low temperature gas in the disc of the galaxy.

The difference between the hot, diffuse halo gas in the region bounded by $10^5 < T(K) < 10^6$ and $\log(n/m_p \text{ cm}^{-3}) < -3.5$ is striking. With local photoionising feedback (LPF), most of the low density gas mass is between 10^5 and 10^6 K. Without LPF, a large fraction of the halo gas has cooled to a phase that is intermediate between the cool, dense disc and the hot, diffuse halo and the gas temperature lies between 10^4 and 10^5 K. Even a small amount of ionising radiation

from the local sources has a big effect on the gas cooling rate, so that gas stays hot longer. The high temperature of the hot halo gas provides pressure support against the galaxy’s gravitational potential and hence reduces the gas accretion rate onto the disc. Thus, there is less gas in the region between the hot, low dense halo gas and the cold dense disc in HM+LPF than in HM.

Another factor that causes more cooling in HM is the positive feedback that the metal enrichment from the higher star formation rate in HM causes. HM starts with a marginally higher accretion rate than HM+LPF, which ejects more metals into the hot halo, which cause the gas to cool faster further enhancing the accretion rate, and consequently makes more stars. The higher halo gas temperature indicates the global nature of LPF and underlines the importance of propagating the radiation field from the local sources throughout the entire volume of the simulation box.

Fig. 10 shows the reduction in gas accretion rate onto the disc more explicitly. The baryonic disc mass evolves similarly in the two simulations until ~ 4 Gyr when they diverge as HM adds mass at a faster rate, leaving HM+LPF lighter than HM. The slope of the baryonic disc mass evolution gives a rough gas accretion rate onto the disc (modulo outflows and stellar accretion). The dot-dash line represents a best linear fit of the gas accretion rate after ~ 4 Gyr. For the HM simulation the slope of this line is $7.25 \text{ M}_\odot \text{ yr}^{-1}$, while the HM+LPF simulation has a slope of $4.10 \text{ M}_\odot \text{ yr}^{-1}$.

The increased cooling rate and equilibrium temperature of the halo gas due to LPF affects star formation by reducing the gas accretion onto the disc. This is different from feedback mechanisms local to star forming events that rely on blowing gas out of the disc. LPF is rather a *preventive* feedback mechanism which reduces the need for artificially high levels of feedback that can destroy the galaxy disc (Agertz et al. 2011; Roškar et al. 2013). LPF also provides a natural and non-violent mechanism to keep the disc lighter and prevent disc instabilities from driving gas to the center.

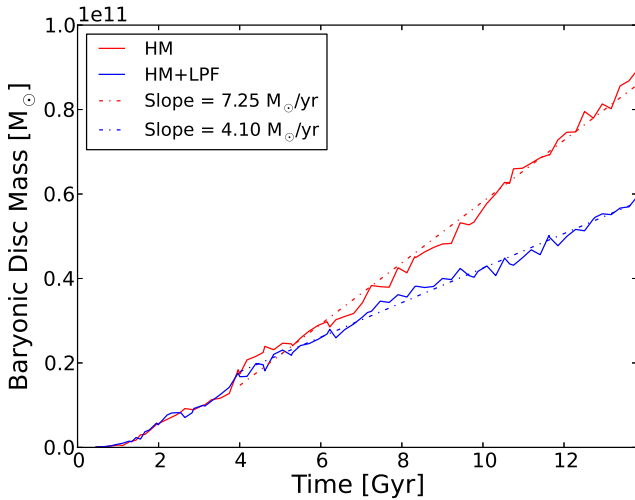


Figure 10. The evolution of the baryonic disc mass of the galaxy as a function of time, for the simulations with (blue curve) and without (red curve) local photoionization.

Fig. 11 shows face-on images of the stellar and gaseous components of the simulated galaxies. The top panels show the stellar distribution and the bottom panels the gas distribution for the HM (left panels) and HM+LPF (right panels) simulations. The HM simulation shows a large stellar bulge and a high concentration of gas in the center. The HM+LPF simulation has a smaller stellar bulge with generally less mass in stars in the disc. The gas distribution in the HM+LPF simulation is more extended and less concentrated than in the HM simulation.

The central concentration of stars and gas in the HM simulation is reflected in the 300 km s^{-1} central peak of the galaxy rotation curve shown in Fig. 12. The HM+LPF simulation creates a slowly rising rotation curve that has a rotation velocity of 200 km s^{-1} from near the center to the edge of the disc, clearly showing that it is much lighter than the HM disc.

The difference in stellar and gaseous distributions and subsequently in the rotation curves can be explained in part due to the reduced gas accretion onto the disc, but also with the reduction in amount of cold gas in the HM+LPF. The HM simulation has a tail of gas at low temperatures ($< 1000 \text{ K}$) and high densities ($n > 1 \text{ cm}^{-3}$). This tail is absent from the HM+LPF run since the additional radiation fields raise the equilibrium temperature of the dense gas. Thus, the average temperature of the disc gas is higher and has higher pressure that stops the disc from fragmenting and forming stars. However, we reiterate that the effect of low energy photons might be overestimated, because we do not impose any criterion for self-shielding in high density gas present in the disc.

8 CONCLUSIONS

We tested a novel method for including the effects of local photoionising radiation fields in galaxy formation simulations. Previously, the expense of including detailed ra-

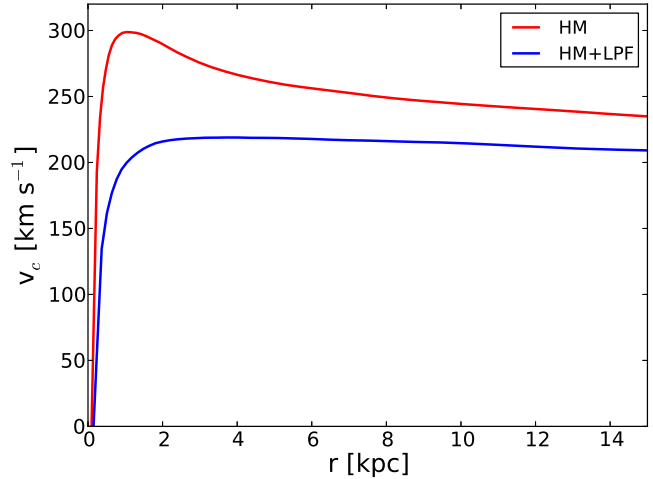


Figure 12. The rotation curves of the galaxy in the HM (red) and HM+LPF (blue) runs at $z = 0$.

diative transfer meant that simulations that tried to include the effect of photoionisation could only be evolved until $z \sim 4$. While such simulations are extremely useful to study the early evolution of the Universe and the reionisation epoch they are not able to address the effect of a local radiation field on galaxy evolution. The local radiation field should have a significant importance in regulating how much gas cools onto discs and fuels star formation. Currently, in many simulations, the only radiation field considered is the UV background against which the galaxy might otherwise be self-shielded (Pontzen et al. 2007; Faucher-Giguère et al. 2009). The local field might be very different from the uniform background and must be included in realistic cosmological simulations of galaxy formation.

Our method uses the existing optimizations that quickly solve gravity to include the r^{-2} attenuation effect, a more detailed description of our method will be presented in Woods et al. (in prep). Our current treatment uses the optically thin limit, which provides an upper limit on the effect of radiation. The optically thin approximation is valid for the x-ray photons that we include in our model of the young star radiation field. X-ray photons are not strongly absorbed in typical ISM conditions. However, we will relax the optical thin approximation in future work.

Our radiation field includes the black body emission from young stars, along with the x-rays that massive stars produce in their winds and supernova explosions, as well as UV flux from post-AGB stars in old stellar populations. Our simple treatment of absorption assumes that 5% of the flux around the Lyman limit escapes from clusters of young stars, while old stars have an escape fraction of unity since they likely moved out of their birth cocoons into an optically thinner environment. Otherwise, the radiation field is only attenuated as an inverse square of distance. These physically motivated assumptions allow us to study the effect of a local ionising radiation field on cooling rates of gas within the galaxy, throughout cosmic time.

As a test of the cooling and to develop physical intuition

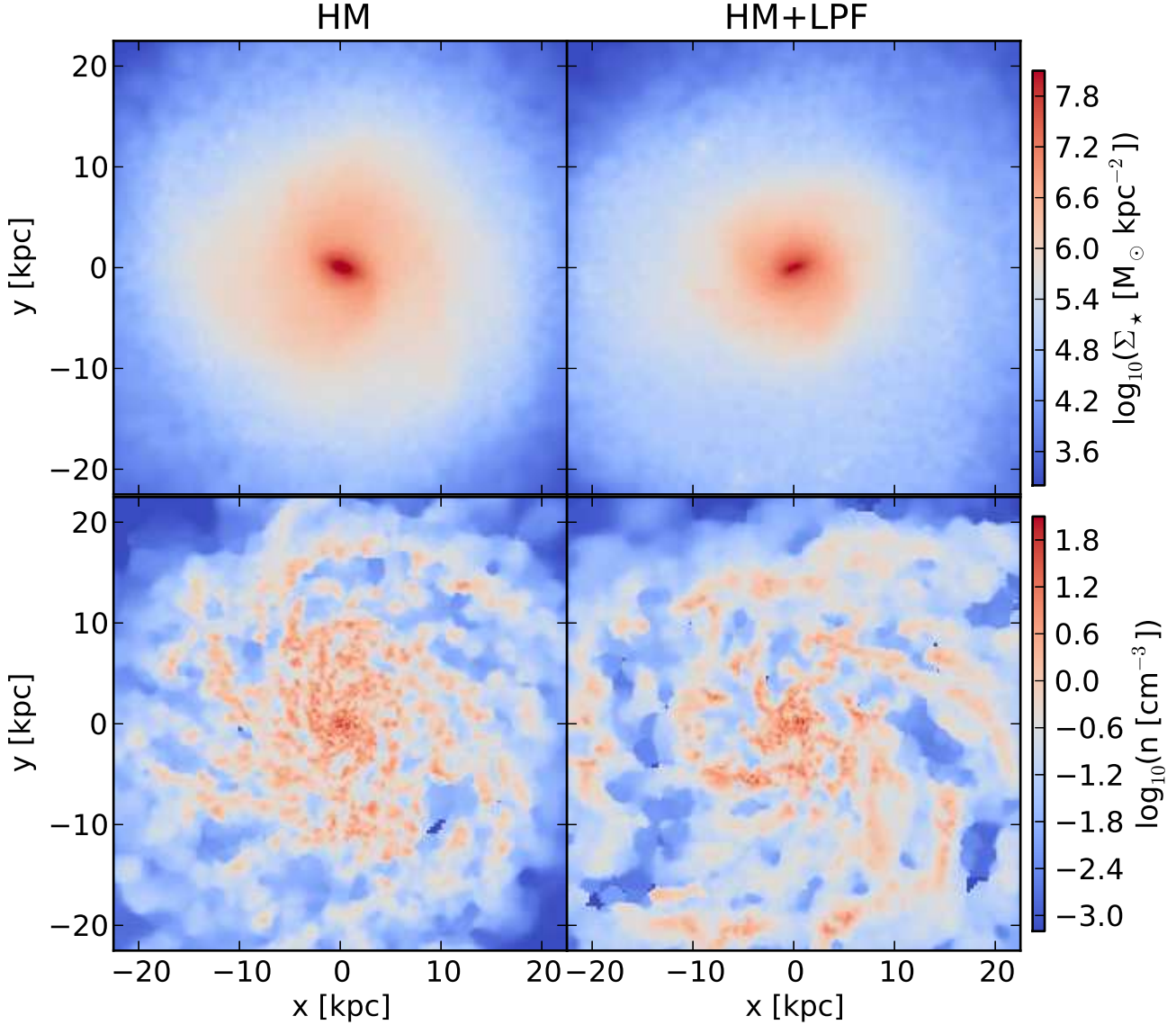


Figure 11. The face on projection view of the stellar (top panels) and gaseous (bottom panels) of the MW like galaxy simulations with the HM (left panels) and HM+LPF (right panels) models.

about how photoionisation affects the cooling rate, we provide simple examples of the evolution of a single gas parcel embedded in the radiation field. We show that a radiation field from young stars that includes soft x-rays can increase the equilibrium temperature of the gas significantly and prolong cooling times (Cantalupo 2010).

We then use our local photoionisation scheme in the SPH code GASOLINE to investigate the effect of local ionising radiation fields in full cosmological simulations of a Milky Way-like galaxy. We simulate the galaxy with and without the local radiation field. We find that the radiation field reduces star formation after $z \sim 1.5$, and results in $\sim 40\%$ less stellar mass. The reduced star formation is due to a combination of factors. The hot, diffuse halo gas surrounding the disc has a higher temperature when the local photoionising field is considered because a small amount of ionising radiation from local sources has a big effect of the gas cooling and

heating rates at low densities, which in turn raises the equilibrium temperature of the gas. This increased temperature of the hot halo gas provides pressure support to the halo gas against the gravitational potential of the galaxy and hence reduces the gas accretion rate onto the disc. This coupling of the local radiation field to the gas cooling in the host galaxy provides a *preventive* feedback mechanism that reduces the gas accretion to the central regions of the galaxy, regulating star formation.

The local ionising radiation field also eliminates high density-low temperature gas by raising the equilibrium temperature of dense gas in the disc. The higher average temperature of the disc gas provides pressure support to the gaseous disc that stops the disc from fragmenting and forming stars. All these effects on the gas distribution by the local radiation field causes the HM+LPF run to form a light and more stable stellar disc, which has a slowly rising rotation curve

which peaks at 200 km s^{-1} , consistent with observations of Milky Way-like galaxies.

We plan to extend this initial study to a broader galaxy mass range (from dwarfs to massive ellipticals) and to improve the parametrization of our radiative transfer scheme in forthcoming work(s). While this result is still preliminary and based on a single simulation, it shows the importance of self-consistently including local photoionisation feedback in simulations aimed at reproducing realistic galaxies.

ACKNOWLEDGEMENTS

The analysis was performed using the `pynbody` package (<http://code.google.com/p/pynbody>), which was written by Andrew Pontzen in addition to the authors. RK, GS and AVM acknowledge financial support through the Sonderforschungsbereich SFB 881 “The Milky Way System” (subproject A1) of the German Research Foundation (DFG). Numerical simulations were performed on the Milky Way supercomputer, funded by the Deutsche Forschungsgemeinschaft (DFG) through Collaborative Research Center (SFB 881) “The Milky Way System” (subproject Z2), hosted and co-funded by the Jülich Supercomputing Center (JSC) along with THEO cluster of the Max-Planck-Institut für Astronomie at the Rechenzentrum in Garching; and the clusters hosted on SHARCNET, part of ComputeCanada. We greatly appreciate the contributions of these computing allocations. JFH acknowledges generous support from the Alexander von Humboldt foundation in the context of the Sofja Kovalevskaja Award. The Humboldt foundation is funded by the German Federal Ministry for Education and Research.

REFERENCES

- Agertz O., Teyssier R., Moore B., 2011, *MNRAS*, 410, 1391
 Altay G., Croft R. A. C., Pelupessy I., 2008, *MNRAS*, 386, 1931
 Altay G., Theuns T., 2013, *MNRAS*, 434, 748
 Anninos P., Zhang Y., Abel T., Norman M. L., 1997, *New Astronomy*, 2, 209
 Bergvall N., Zackrisson E., Andersson B.-G., Arnberg D., Masegosa J., Östlin G., 2006, *A&A*, 448, 513
 Binney J., 1977, *ApJ*, 215, 483
 Brook C. B., Stinson G., Gibson B. K., Shen S., Macciò A. V., Wadsley J., Quinn T., 2013, *arXiv:1306.5766*
 Bruzual G., Charlot S., 2003, *MNRAS*, 344, 1000
 Cantalupo S., 2010, *MNRAS*, 403, L16
 Cerviño M., Mas-Hesse J. M., Kunth D., 2002, *A&A*, 392, 19
 Ceverino D., Klypin A., Klimek E., Trujillo-Gomez S., Churchill C. W., Primack J., Dekel A., 2013, *arXiv:1307.0943*
 Chabrier G., 2003, *PASP*, 115, 763
 Code A. D., 1969, *PASP*, 81, 475
 Efstathiou G., 1992, *MNRAS*, 256, 43P
 Faucher-Giguère C.-A., Lidz A., Zaldarriaga M., Hernquist L., 2009, *ApJ*, 703, 1416
 Ferland G. J., Korista K. T., Verner D. A., Ferguson J. W., Kingdon J. B., Verner E. M., 1998, *Publ. Astron. Soc. Pac.*, 110, 761
 Fumagalli M., Prochaska J. X., Kasen D., Dekel A., Ceverino D., Primack J. R., 2011, *MNRAS*, 418, 1796
 Gnat O., Ferland G. J., 2012, *ApJS*, 199, 20
 Gnedin N. Y., 2008, *ApJL*, 673, L1
 Gnedin N. Y., Hollon N., 2012, *ApJS*, 202, 13
 Grimes J. P. et al., 2009, *ApJS*, 181, 272
 Grimm H.-J., Gilfanov M., Sunyaev R., 2003, *MNRAS*, 339, 793
 Haardt F., Madau P., 2012, *ApJ*, 746, 125
 Heckman T. M., Dahlem M., Lehnert M. D., Fabbiano G., Gilmore D., Waller W. H., 1995, *ApJ*, 448, 98
 Iliev I. T. et al., 2009, *MNRAS*, 400, 1283
 Jimenez R., Flynn C., MacDonald J., Gibson B. K., 2003, *Science*, 299, 1552
 Kaviraj S. et al., 2007, *ApJS*, 173, 619
 Kroupa P., 2001, *MNRAS*, 322, 231
 Leitherer C. et al., 1999, *ApJS*, 123, 3
 Mo H., van den Bosch F. C., White S., 2010, *Galaxy Formation and Evolution*
 Nestor D. B., Shapley A. E., Kornei K. A., Steidel C. C., Siana B., 2013, *ApJ*, 765, 47
 Oppenheimer B. D., Schaye J., 2013a, *MNRAS*, 434, 1063
 Oppenheimer B. D., Schaye J., 2013b, *MNRAS*, 434, 1043
 Pawlik A. H., Schaye J., 2008, *MNRAS*, 389, 651
 Persic M., Rephaeli Y., Braito V., Cappi M., Della Ceca R., Franceschini A., Gruber D. E., 2004, *A&A*, 419, 849
 Petkova M., Springel V., 2011, *MNRAS*, 412, 935
 Pontzen A., Hewett P., Carswell R., Wild V., 2007, *MNRAS*, 381, L99
 Rahmati A., Schaye J., Pawlik A. H., Raičević M., 2013, *MNRAS*, 431, 2261
 Rees M. J., 1986, *MNRAS*, 218, 25P
 Rees M. J., Ostriker J. P., 1977, *MNRAS*, 179, 541
 Roškar R., Teyssier R., Agertz O., Wetzstein M., Moore B., 2013, *arXiv:1308.6321*
 Shapley A. E., Steidel C. C., Pettini M., Adelberger K. L., Erb D. K., 2006, *ApJ*, 651, 688
 Shen S., Wadsley J., Stinson G., 2010, *MNRAS*, 407, 1581
 Siana B. et al., 2007, *ApJ*, 668, 62
 Steidel C. C., Pettini M., Adelberger K. L., 2001, *ApJ*, 546, 665
 Stinson G., Seth A., Katz N., Wadsley J., Governato F., Quinn T., 2006, *MNRAS*, 373, 1074
 Stinson G. S., Bailin J., Couchman H., Wadsley J., Shen S., Nickerson S., Brook C., Quinn T., 2010, *MNRAS*, 408, 812
 Stinson G. S., Brook C., Macciò A. V., Wadsley J., Quinn T. R., Couchman H. M. P., 2013, *MNRAS*, 428, 129
 Strickland D. K., Heckman T. M., Colbert E. J. M., Hoopes C. G., Weaver K. A., 2004, *ApJS*, 151, 193
 Vogelsberger M., Genel S., Sijacki D., Torrey P., Springel V., Hernquist L., 2013, *arXiv:1305.2913*
 Wadsley J. W., Stadel J., Quinn T., 2004, *New Astronomy*, 9, 137
 White S. D. M., Rees M. J., 1978, *MNRAS*, 183, 341
 Wiersma R. P. C., Schaye J., Smith B. D., 2009, *MNRAS*, 393, 99